ARTICLE

Bioinspired iron-loaded polydopamine nanospheres as green flame retardant for epoxy resin via free radical scavenging and catalytic charring

Received 00th January 20xx,
Accepted 00th January 20xx

DOI: 10.1039/x0xx00000x

Lu Zhang, [a,b] Qi Wang, [a,b] Rong-Kun Jian, [a,c] and De-Yi Wang [a]*

The versatile coating capability of polydopamine (PDA) has received much research interest in numerous fields, including flame retardant functionalization of fillers for polymers. However, the understanding of flame retardant actions of PDA materials in combustion still remains incomplete, limiting its practical applications and future designs as polymer reinforcing fillers. In this work, iron-loaded polydopamine (Fe-PDA) nanospheres were introduced into epoxy resin (EP) as green flame retardant additives. The resultant EP nanocomposites exhibited remarkably reduced flammability, reflected by the high LOI value of 31.6%, V-0 rating in UL-94 test, as well as a 41% reduction of the peak heat release rate at 5 wt% Fe-PDA loading. More importantly, for the first time, it is clearly revealed that the flame inhibition action in gas phase was owing to the free radical scavenging ability of Fe-PDA. In addition to the gas phase action, Fe-PDA also promoted the charring process in condensed phase, leading to the formation of integrated char layers which effectively delayed the mass and heat transfer of combustion. Based on these actions (free radical scavenging and catalytic charring), Fe-PDA acted as the nontoxic and highly efficient flame retardant in EP.

1. Introduction

Dopamine, a natural material inspired by marine mussel byssus, has received a fair amount of attention since its versatile adhesive capabilities were reported in 2007.[1,2] Under an alkaline environment, dopamine can spontaneously polymerize and form a thin polydopamine (PDA) layer on various surfaces.[3,4] The material-independent surface coating capability of PDA have been used in many fields, including surface engineering of fillers for polymer composites.[5–10] For instance, PDA could be coated on graphene,[11] clays,[12] glass fibers,[13] and hence, to improve interactions between the fillers and polymer matrix.

In addition to its unique adhesive properties, dopamine can be directly polymerized into nanoparticles without the use of template.[14] These melanin-like nanoparticles have proved to be appealing materials used in biomedical,[15] catalysis,[16] and free radical quenching.[17] Besides, transition-metal containing PDA bulk materials could be formed if transition-metal ions, such as Fe^{3+}, Mn^{3+}, Ni^{2+}, were added into the reaction media used for dopamine polymerization.[18–20] It is also suggested that metal complexes can be better free radical scavengers than the parent ligand materials.[21,22] Moreover, transition metal compounds, especially iron compounds, was found to efficiently catalyse the charring process of polymer materials (e.g., epoxy resin) during combustion.[23]

It is always challenging but desirable to develop nontoxic and highly efficient flame retardants for polymer composites, in order to reduce the occurrence of fire accidents and fire-related fatalities. PDA, as well as PDA/graphene oxide (GO) nanocoatings have been applied on macroporous flexible polyurethane (PU) foam to obtain coated PU foam with high flame retardancy.[24,25] It is suggested that the char formation and free radical scavenging actions of PDA coatings enabled the flame retardant foams with a reduced peak heat release rate. By the surface PDA coating, highly flame retardant sponges,[26,27] cotton fabrics,[28,29] and flexible film[30] were also successfully prepared. In our group, with the assistance of PDA layer, halloysite nanotubes,[31] boron nitride nanosheets[32] and flax fibers[33] have been functionalized to prepare polymer composites with significantly enhanced flame retardancy. However, it is worth noting that, instead of being the functional flame retardant additives, the thin PDA coatings were mainly exploited as a versatile platform for further functionalization of the fillers. It was mainly the fillers, as well as the coated flame retardants, which exhibited the flame retardant actions in polymer composites.

Generally, it is considered that flame retardants act chemically and/or physically in the gas and/or condensed phase.[34–36] The Fe(III)-chelated PDA material, which is intrinsically eco-friendly and biocompatible, with high free radical scavenging and catalytic carbonization abilities, might play the role of an efficient flame retardant in both gas and

[a] IMDEA Materials Institute, Calle Eric Kandel, 2, 28906 Getafe, Madrid, Spain. Email address: deyi.wang@imdea.org.
[b] E.T.S. de Ingenieros de Caminos, Universidad Politécnica de Madrid, Calle Profesor Aranguren 3, 28040 Madrid, Spain.
[c] College of Chemistry and Materials Science, Fujian Normal University, Shangsan Road 8, 350007 Fuzhou, Fujian, China.

† Footnotes relating to the title and/or authors should appear here.
Electronic Supplementary Information (ESI) available: [details of any supplementary information available should be included here]. See DOI: 10.1039/x0xx00000x

condensed phase. With this point of view, the facile one-pot synthesized iron-loaded PDA (Fe-PDA) nanospheres were adopted as the flame retardants for epoxy resin (EP). To investigate the influence of free radical scavenging ability on the flame retardant effectiveness, a commercially available, phosphorus-containing flame retardant (9,10-dihydro-9-oxa-10-phosphaphenanthrene-10-oxide, designated as DOPO) was used to modify Fe-PDA by the one step Atherton-Todd reaction (DOPO@Fe-PDA), in order to alter its free radical scavenging ability.[37,38] The free radical scavenging ability of Fe-PDA and DOPO@Fe-PDA, as well as the flame retardancy of corresponding EP composites were investigated to prove the hypothesis: the free radical scavenging action contributes to the extinguishment of flame in gas phase. In addition, detailed analysis of char residues after cone calorimeter test were performed to investigate the catalytic charring capabilities of Fe-PDA in EP composites.

2. Experimental

2.1 Materials

Iron (III) chloride hexahydrate ($FeCl_3·6H_2O$), dopamine hydrochloride, Tris(hydroxymethyl)aminomethane (Tris), Dichloromethane (CH_2Cl_2), Carbon tetrachloride (CCl_4), Triethylamine (Et_3N), ethanol (absolute alcohol, ≥98%) and 4,4'-Diaminodiphenylmethane (DDM) were purchased from Sigma-Aldrich. 2,2-Diphenyl-1-picrylhydrazyl (free radical, DPPH) was purchased from Alfa Aesar. DOPO was provided by TCI Chemicals Company. Epoxy resin (Epoxydharz C) was supplied from R&G Faserverbundwerkstoffe GmbH. Deionized water was obtained from the water purification system by our laboratory.

2.2 Synthesis of Fe-PDA nanospheres

Fe-PDA nanospheres were prepared using the previously reported method with slight modifications.[39] In brief, 2 g dopamine hydrochloride (10.5 mmol) was firstly dissolved in 1000 mL DI water. 0.95 g $FeCl_3·6H_2O$ (3.52 mmol) and 2.42 g Tris (20 mmol) were then added into the solution. The mole ratio between dopamine hydrochloride and Fe^{3+} was 3:1. Tris provided the alkaline environment and stabilized the PH value during reaction. The reaction mixture was continuously stirred under room temperature for 48 h. The black solid products (Fe-PDA) were gathered by centrifugation and rinsed by deionized water and ethanol at least three times before drying in a vacuum oven at 60 °C. To verify the monodisperse of iron element in Fe-PDA nanospheres, carbonized samples (Fe/C-PDA) were obtained in a tube furnace at 650 °C for 2 h under argon atmosphere. Fe/C-PDA-2.5, Fe/C-PDA-5 and Fe/C-PDA-10 represent samples carbonized under different heating rates (2.5, 5 and 10 °C/min, respectively).

2.3 Synthesis of DOPO@Fe-PDA nanospheres

2.5 g Fe-PDA was firstly added into 20 mL dichloromethane. The mixture was continuously stirred for 30 min and followed by 15 min ultrasonic treatment to prevent the aggregation of nanospheres. Then excess DOPO (5 g, 23.1 mmol) and Et_3N (3.2 mL, 23.1 mmol) were dissolved in the above mixture, stirred and cooled to 5 °C with an ice bath. After cooling down, CCl_4 (2.2 mL, 23.1 mmol) dissolved in 10 mL dichloromethane, was added dropwise to ensure that the reaction temperature did not exceed 10 °C. After the addition was complete, the reaction was allowed to warm up to room temperature and the stirring was continued for 10 h. The reaction mixture was washed three times with water and ethanol separately to remove the excess initial reactants and triethylamine hydrochloride by centrifugation. Finally, the product (DOPO@Fe-PDA) was obtained after drying overnight in a vacuum oven at 60 °C.

2.4 Preparation of EP nanocomposites

Different loadings of Fe-PDA (1, 3 and 5 wt%) and 3 wt% DOPO@Fe-PDA were adopted to prepare EP nanocomposites. The typical preparation process of composite containing 3 wt% Fe-PDA (EP/3Fe-PDA) is illustrated below: Firstly, 3 g Fe-PDA was firstly added into 30 mL acetone under ultrasonic treatment for 30 min. Then 75.7 g EP was added into the suspension with 1 h mechanical stirring. To fully remove the acetone, the above mixture was heated to 70 °C under rotary vacuum evaporator for at least 4 h. After that, 21.3 g DDM was added into the mixture at 90 °C under stirring. Finally, the obtained EP composite (100 g) was cured in a silicone mould at 100 and 150 °C for 2 h, respectively. The preparation of neat EP and other EP composites followed a similar procedure, except the amount and type of fillers. The full experimental design from synthesis of Fe-PDA nanospheres to preparation of EP nanocomposites is illustrated in **Scheme 1**.

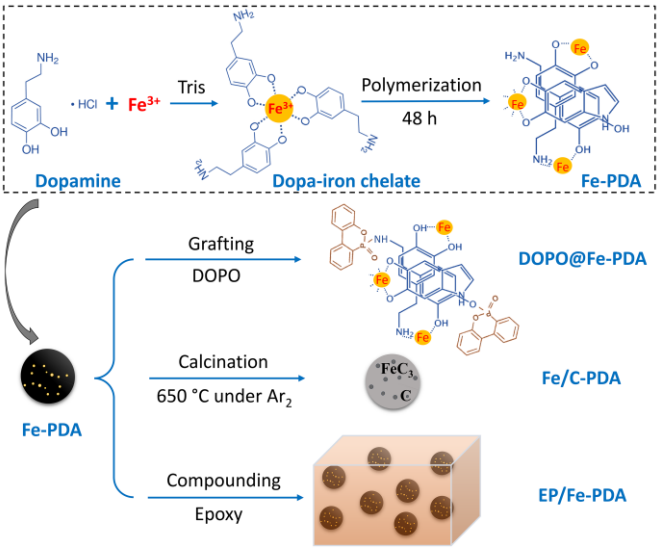

Scheme 1. Scheme illustration of the preparation of Fe-PDA and its derived materials.

2.5 Measurements

X-ray diffraction (XRD) pattern was collected on Philip X' Pert PRO diffractometer using a Cu Kα radiation. Fourier transform infrared spectroscopy (FT-IR) spectra was obtained on the Nicolet iS50 spectrometer. The morphologies of fillers, composite fracture surfaces and char residues were studied by FEI Helios NanoLab 600i microscope. High resolution transmission electron microscopy (HRTEM), selected area

electron diffraction (SAED) and energy dispersive X-ray spectrometry (EDS) mapping were implemented by FEI Talos F200X scanning/transmission electron microscope. Thermogravimetric analysis (TGA) was conducted by the thermal gravimetric analyzer (TA Q50), with a heating rate of 10 °C/min. X-ray photoelectron spectroscopy (XPS) was performed on VG ESCALAB MK II spectrometer by Al Kα line (hv = 1486.6 eV). TG-FTIR was conducted by FT-IR spectrometer connected with TG analyzer through a heated pipe. The evolved volatiles were directed to gas chamber for FT-IR measurement. Non-isothermal DSC test of the curing reaction of EP and its nanocomposites was carried by differential scanning calorimeter (TA Q200) from 0 to 280 °C, with a heating rate of 10 °C/min in N_2 atmosphere. Fe(III) concentration was determined by ICP-OES test. The metal was first stripped from Fe-PDA by HNO_3 in water, then quantified by inductively coupled plasma optical emission spectrometry (ICP-OES, Varian Vista Pro) in Universidad Rey Juan Carlos, Madrid.

The electron paramagnetic resonance spectrometer (EPR, Bruker A200) was used to study the EPR characteristics of the synthesized nanoparticles. The experiments were carried out at room temperature with a 9.64 GHz microwave frequency, 10 mW microwave power and 2 G modulation amplitude. DPPH free radical scavenging activity of the nanomaterials was measured according to the previously reported method.[17,40] Firstly, 0.1 mM of DPPH solution in ethanol was freshly prepared. Then 200 µL ethanol solution containing 40 and 80 µg Fe-PDA (or DOPO@Fe-PDA) was mixed with 4 mL DPPH solution. After 20 min in the dark, UV–Vis spectrum of the sample solutions was measured between 200–800 nm by UV-2600 Shimadzu spectrophotometer. The radical scavenging activity (*I*) was derived from the change of absorbance values at 516 nm, given by $I = [1 - (Ai - Aj)/Ac] \times 100\%$, where *Ac* and *Ai* were the absorbance values of DPPH solution in the absence and presence of the samples, respectively, *Aj* was the absorbance of samples in ethanol without DPPH.

Limiting oxygen index (LOI) values were obtained by the FTT (Fire Testing Technology, UK) instrument according to ASTM D2863. UL-94 vertical burning test was performed using the FTT instrument according to ASTM D3801. Cone calorimeter test (CCT) was conducted with FTT Cone Calorimeter following ISO 5660-1 under an external heat flux of 50 kW/m^2; the size of specimen was 100 × 100 × 4 mm^3 and each sample was tested twice under the same conditions. Tensile test was performed on the universal electromechanical testing machine (INSTRON 3384, Instron) according to standard ASTM D638 with a crosshead speed of 1 mm/min. Dynamic mechanical analysis (DMA) was operated on the Q800 DMA (TA Instruments, USA) from room temperature to 220 °C at a heating rate of 3 °C/min.

3. Results and discussion

3.1 Characterization of Fe-PDA and its derived nanomaterials

The obtained Fe-PDA nanomaterials were characterized by scanning electron microscopy (SEM) and transmission electron microscopy (TEM) to quantify the morphology and element composition. As shown in **Figure 1**, Fe-PDA particles are uniformly spherical in shape, with diameters ranging from 80 to 140 nm. The selected area high-angle annular dark field (HAADF) coupled with energy-dispersive X-ray spectroscopy (EDS) proves the existence of Fe, N and O element in the nanospheres (**Figure 1e**). The atomic ratio of Fe to N is 1:4.1, which represents the ratio between Fe^{3+} (molecule weight 56 g/mol) and dopamine structure (molecule weight 153 g/mol), indicating approximately 8.2 wt% of iron element in Fe-PDA nanospheres. ICP-OES results indicate the Fe(III) concentration is 8.10±0.03 wt% in Fe-PDA. Meanwhile, as shown in **Figure S1**, after thermal decomposition in air, the remaining weight percentage of red-brown solid (mainly iron(III) oxide, with a molecule weight of 80 g/mol)[41] is 12.6 wt% at 700 °C, indicating 8.8 wt% of iron in Fe-PDA, which is close to the EDS and ICP-OES results.

XPS analysis was employed to analyse the elemental chemical

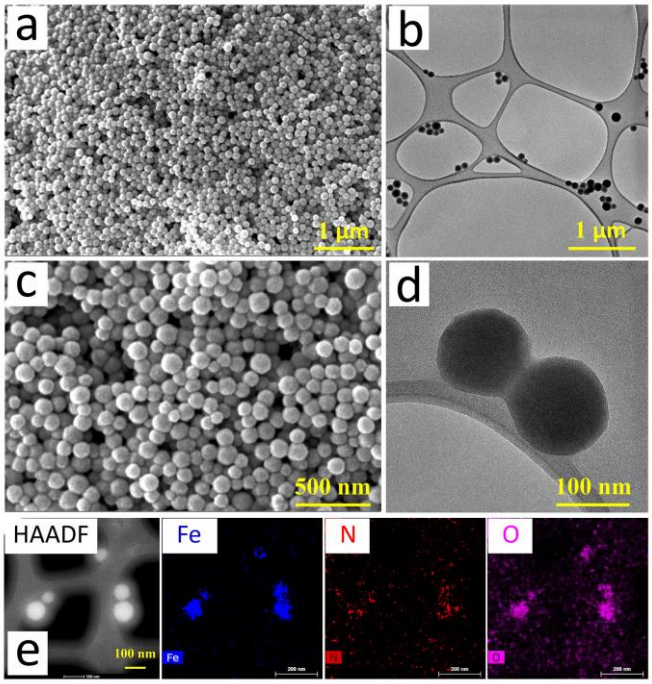

Figure 1. (a,c) SEM images, (b,d) TEM images, (e) HAADF image and the corresponding element mappings of Fe-PDA nanospheres.

states in Fe-PDA. **Figure 2a** shows the survey spectra of Fe-PDA, revealing the presence of Fe, N, O, as well as C in the nanospheres. The Fe 2p spectrum (**Figure 2b**) can be divided into two peaks with the binding energies of 724.8 and 711.2 eV, corresponding to Fe $2p_{1/2}$ and Fe $2p_{3/2}$, respectively. According to previous literatures, these peak locations (724.8/711.2 eV) indicate the iron element in Fe-PDA mainly exists in the ferric state, not ferrous state.[42,43] The two dominant intensities (**Figure 2c**) at 400.4 and 398.8 eV deconvolved from the N 1s peak are attributed to N–H and N=C respectively,[44] proving the abundant amino groups at the surface of Fe-PDA, which might facilitate the interactions between nanospheres and EP matrix. Moreover, the deconvolution of O 1s peak in **Figure 2d** exhibits O=C (533.2 eV), O–C (531.6 eV) and O–Fe (529.9 eV) signals,[45] indicating the coordination bonds between ferric ions and catechol groups from surface of PDA.

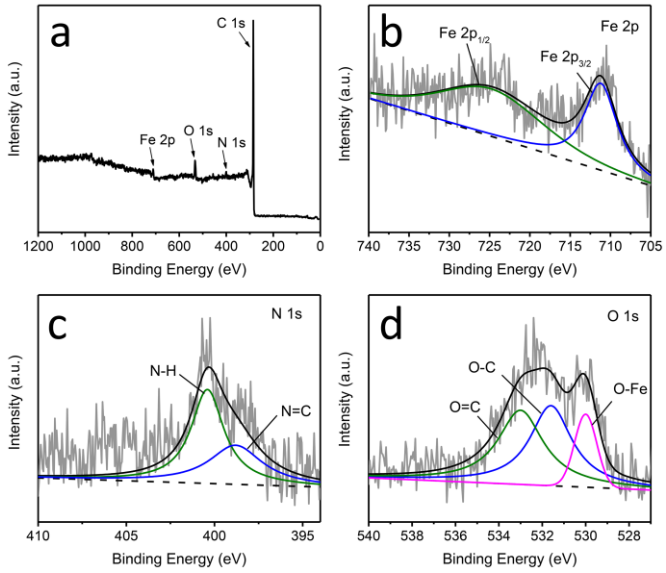

Figure 2. (a) XPS survey spectra of Fe-PDA and the corresponding high-resolution XPS spectra of (b) Fe 2p, (c) N 1s and (d) O 1s.

The structure of PDA materials has proved difficult to unambiguously elucidate, and different molecular models have been proposed.[46,47] In this study, to verify that Fe(III) is continuously incorporated into the Fe-PDA as it forms, not merely being chelated at the surface, distribution of iron element in the carbonized samples (Fe/C-PDA) were studied under TEM. As shown in **Figure 3a-c,** after calcination, the ultrafine iron containing particles (average size less than 10 nm) are evenly embedded throughout the Fe/C-PDA-2.5 nanospheres, indicating a uniform distribution of iron in the original Fe-PDA. The HRTEM image (**Figure 3d**) of the ultrafine particle shows the lattice fringe with a plane spacing of 0.21 nm, corresponding to the (211) lattice plane of Fe_3C. The SAED pattern (**Figure 3e**) and XRD analysis (**Figure 3f**) confirm the formation of Fe_3C and graphitic carbon in Fe/C-PDA-2.5. Additionally, it is interesting to note that the heating rate in calcination process greatly influences the structure of carbonized samples. Under the fast heating rates (5 and 10 °C/min), the obtained Fe/C-PDA-5 and Fe/C-PDA-10

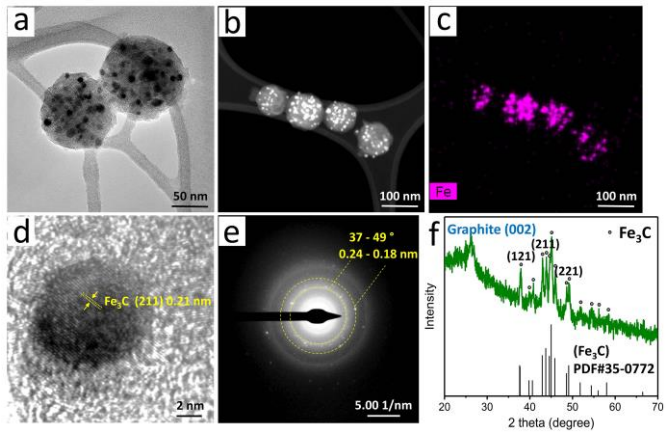

Figure 3. (a) TEM image, (b) HAADF image, (c) Fe element mapping, (d) HRTEM image, (e) SAED pattern and (f) XRD spectrum of carbonized Fe/C-PDA-2.5 nanospheres.

nanospheres show much larger and irregular iron containing particles (**Figure S2**).

DOPO@Fe-PDA was synthesized via the Atherton-Todd reaction among –OH, $–NH_2$ in Fe-PDA and P–H in DOPO. It was characterized by TEM, FT-IR spectroscopy, TGA, and EPR spectroscopy. TEM image (**Figure S3**) shows that DOPO@Fe-PDA preserves the spherical morphology. The element mapping and EDS analysis confirm the existence of P element in DOPO@Fe-PDA nanospheres. As shown in **Figure 4a,** the IR spectrum of Fe-PDA shows adsorption peaks at 1596, 1467 cm^{-1} and 1371, 1298 cm^{-1}, which can be attributed to its indole and phenolic groups, respectively.[48,49] New peaks at 1440, 1202 and 759 cm^{-1} assigned to P-Ph, P=O and P–O–Ph, respectively, are clearly observed in DOPO@Fe-PDA.[50,51] Meanwhile, the absorption peak at around 2434 cm^{-1}, which is assigned to the P-H bond in DOPO, disappears in spectrum of DOPO@Fe-PDA, indicating the successful reaction among P–H in DOPO and phenolic hydroxyl/amino groups in Fe-PDA.[52] DOPO@Fe-PDA exhibits a significantly higher thermal stability compared to Fe-PDA (**Figure 4b**), which is attributed to the formation of more thermally stable phosphonate/phosphonamidate derivatives.[53] EPR spectra of the samples were collected at room temperature (**Figure 4c**). The two samples show similar EPR curves, with a wide peak at 1580 G (g = 4.3) which is assigned to the high-spin Fe(III) in sites of low symmetry. Meanwhile, a very broad spectrum centered at 3280 G (g = 2.1) is clearly observed, indicating a high iron loading level in the nanomaterials.[54] The characteristic free radical signal of polydopamine materials cannot be observed, which is likely owing to the high loading level of Fe(III). As previously reported, the magnetic interaction between paramagnetic transition metal ions and free radicals leads to a loss of EPR signal amplitude in melanin-like materials.[55]

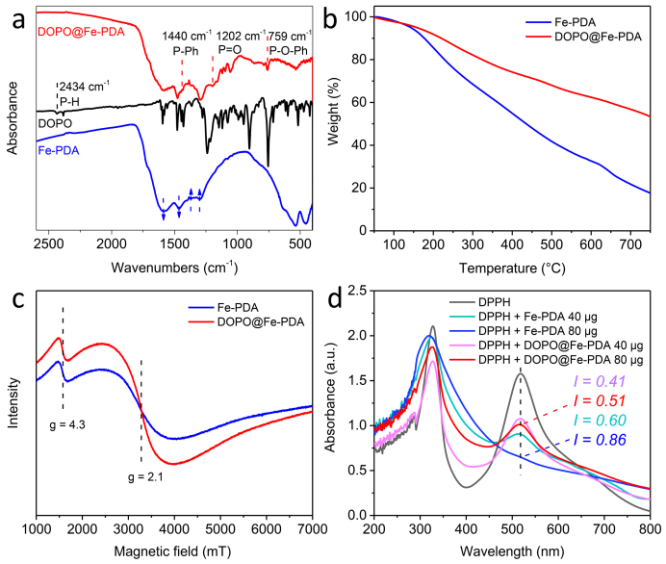

Figure 4. (a) FT-IR spectrums, (b) TGA curves, (c) EPR spectrums and (d) UV–Vis spectral change upon addition of Fe-PDA and DOPO@Fe-PDA in DPPH assay.

The radical scavenging capability of Fe-PDA and DOPO@Fe-PDA was further investigated by employing DPPH assay along with UV–Vis spectroscopy. By monitoring the decline in

absorbance at 516 nm corresponding to DPPH free radicals, the radical scavenging activity of the prepared nanomaterials can be evaluated. **Figure 4d** shows that the absorbance at 516 nm decreased with the addition of synthesized nanoparticles to DPPH solution. The absorbance signal nearly disappeared when 80 μg Fe-PDA was added into the DPPH solution. The calculated radical scavenging activity of DOPO@Fe-PDA (41% at 40 μg and 51% at 80 μg) is significantly lower compared to that of Fe-DPA (60% at 40 μg and 86% at 80 μg). The high radical scavenging capability of Fe-PDA is mainly attributed to its unique catecholamine moieties.[56] The Atherton-Todd reaction greatly consumes the catecholamine groups at surface of Fe-PDA, thus effectively decreasing its ability to scavenge free radicals.

3.2 Thermal analysis of EP/Fe-DPA composites

The thermal stability of EP/Fe-DPA composites, as well as the catalytic charring ability of Fe-PDA in EP was studied by thermogravimetric analysis (TGA) under nitrogen atmosphere. As shown in **Figure 5,** the addition of Fe-PDA decreased the onset degradation temperature (temperature at 5% weight loss) of EP. According to previous TGA results (**Figure 4b**), the high iron loading Fe-PDA shows a weight loss of around 40 wt% at 340 °C (which is the onset degradation temperature of EP) in nitrogen atmosphere. The active radicals decomposed from Fe-PDA might subsequently attack the polymer substrate, thus decreasing its onset degradation temperature.[57,58] In terms of char yield at 700 °C, EP/Fe-PDA possessed significantly higher residue weights compared to neat EP. Notably, the residue weight of EP increased from 16.3 to 20.2 wt% with the addition of 1 wt% nanofillers, which demonstrated the strong catalytic charring ability of Fe-DPA in EP system. The maximum weight derivation of EP decreased from 2.45 to 1.62, 1.56, and 1.80 wt%/°C with the increasing Fe-PDA loading (1, 3 and 5 wt%, respectively). It is found that the maximum weight derivation was not further decreased with a higher Fe-PDA loading. And in the meanwhile, with additional Fe-PDA in EP, the char yield at 700 °C increased merely from 22.0 (EP/3Fe-PDA) to 22.9 wt% (EP/5Fe-PDA). These results suggested that an excess amount of Fe-DPA in EP did not contribute to higher charring efficiency. On one side, it could be due to the aggregation of Fe-PDA nanospheres in EP matrix at a high loading level. On the other side, the catalyst charring efficiency might be decreased when the amount of metallic catalysis was above the maximum effective loading. Fe-PDA might behave more like the "accelerator" than "retarder" in the decomposition of epoxy at a high loading level.[59]

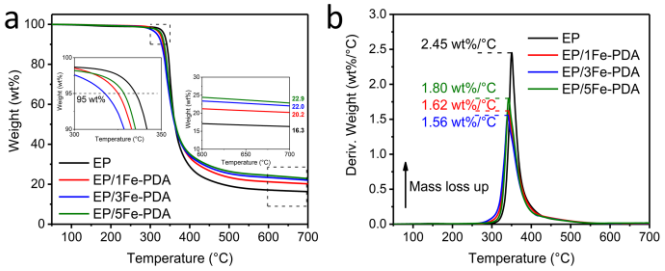

Figure 5. (a) TGA and (b) DTG curves of EP and its nanocomposites.

3.3 Fire behaviour of EP/Fe-DPA composites

The LOI and UL-94 tests were used to evaluate the flammability of EP/Fe-PDA composites in small-scale fire test conditions. As shown in **Table 1**, neat EP owned a low LOI value of 25.6%. The addition of Fe-PDA significantly increased the LOI value of EP composites, even at a low loading level. Neat EP burned fiercely once ignited in UL-94 test. EP/Fe-PDA showed notably improved ability to self-extinguish after the ignition flame was removed. EP composites with 1 and 3 wt% Fe-PDA were rated as V-1, and further to V-0 with 5 wt% additive. The low flammability displayed by EP/Fe-PDA in LOI and UL-94 tests was mainly attributed to the flame inhibition effect in gas phase. More specifically, during the combustion, Fe-PDA owned the ability to scavenge nearby free radicals that typically evolved extra fuel for the flame as they attack polymer materials. As a proof of the free radical scavenging action, the LOI value of EP/3DOPO@Fe-DPA was 27.3%, evidently lower than 30.5% of EP/3Fe-DPA. In the meanwhile, EP with 3 wt% DOPO@Fe-DPA showed no rating in UL-94. The decreased flame retardant efficiency well corresponded to the declined radical scavenging capability of DOPO@Fe-PDA in comparison with Fe-PDA. In addition to the radical scavenging activity in gas phase, the catalytic charring effect in condensed phase also contributed to the improved flame retardancy of EP/Fe-PDA composites. The intensive carbonaceous layers at surface of specimens well protected the underlying materials during combustion, thus facilitating the extinguishment of flame.

Table 1. LOI and UL-94 results of EP and its nanocomposites.

Sample	UL-94 rating	t1/t2[a] (s)	LOI (%)
EP	No rating	>30/-[b]	25.6
EP/1Fe-DPA	V-1	20/8	28.5
EP/3Fe-DPA	V-1	15/3	30.5
EP/5Fe-DPA	V-0	5/1	31.6
EP/3DOPO@Fe-DPA	No rating	>30/-[b]	27.3

[a] t1/t2: average flame time after the first/second time ignition;

[b] -: no second time ignition applied.

For a more detailed study of flame retardancy, cone calorimeter test was carried out for EP/Fe-PDA samples. The heat release rate (HRR), total heat release (THR), total smoke release (TSR) and residue weight curves are displayed in **Figure 6**. As shown in **Figure 6a,** neat EP exhibited a sharp peak heat release rate (pHRR) at 1285±32 kW/m^2. In the presence of Fe-PDA, the pHRR dropped distinctly to 1023±41, 780±19 and 760±29 kW/m^2 for EP/1Fe-PDA, EP/3Fe-PDA and EP/5Fe-PDA, respectively. In contrast to EP with a continuously rising heat release rate, the flame retardant composites experienced an obvious drop before reaching to the peak, which was due to the build-up of carbonaceous layers during combustion. The char layers acted as a physical barrier which slowed down the transmission of oxygen and volatiles, thus effectively decreasing the heat release rate of burning composites. No sharp heat release rate peaks were observed for EP/3Fe-PDA and EP/5Fe-PDA, which indicated the formed char layers were robust enough to protect the underlying materials. In addition,

the total heat release of EP composites was gradually reduced with the increasing loading level of Fe-PDA (**Figure 6b**). This can be explained by the enhanced char formation and decreased amount of fuel supply in EP/Fe-PDA system. Meanwhile, in **Figure 6c**, EP/3Fe-PDA displayed a 17% decrease in total smoke release compared to neat EP. Similar to the TGA results, an increased residue weight was observed for EP with Fe-PDA (**Figure 6d**), which was in accordance with the enhanced charring ability of EP/Fe-PDA composites. Based on these results, it was concluded that Fe-PDA nanospheres showed a high flame retardant efficiency in EP matrix. It is worth mentioning that, EP/3Fe-PDA and EP/3DOPO@Fe-PDA showed a similar HRR curves (**Figure S4a**), as well as the similar TGA curve in N_2 atmospheres (**Figure S5**). The free radical scavenging ability did not exhibit an obvious influence on the heat release rate. However, more smoke production was observed for EP/3DOPO@Fe-PDA compared to EP/3Fe-PDA (**Figure S4b**), further demonstrating the low performance of DOPO@Fe-PDA as flame retardant in EP.

The gaseous products released during the thermal decomposition of EP and EP/3Fe-PDA were characterized by TG-FTIR. **Figure 7a** showed the Gram–Schmidt curves

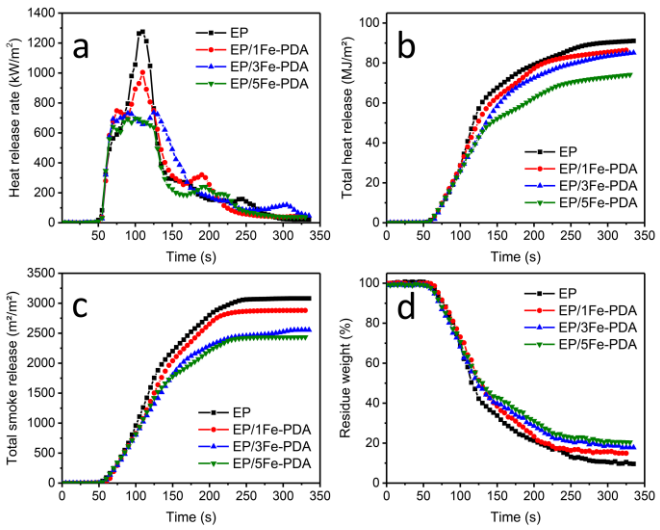

Figure 6. (a) HRR, (b) THR, (c) TSR and (d) residue weight vs time curves of EP and its nanocomposites.

corresponding to TG-FTIR analysis of EP and EP/3Fe-PDA. The peak area after base line correction was calculated to be 3.3 and 2.1 for EP and EP/3Fe-PDA, respectively. The decreased peak area qualitatively reflected less gaseous products were released from EP/3Fe-PDA, which was consistent with the reduced maximum weight derivation in DTG curves.[60] The detailed FTIR spectra of evolved gaseous products at different decomposition stages are displayed in **Figure 7b-d**. The similar FTIR spectra for EP and EP/3Fe-PDA at the maximum decomposition stage indicated the addition of Fe-PDA did not greatly alter the thermal decomposition route of EP. While obviously strengthened peaks at 1261 and 1177 cm^{-1} were observed for EP/3Fe-PDA at the initial and growing decomposition stages. Those two peaks for EP/3Fe-PDA at initial decomposition stage were mainly assigned to the stretching vibrations (1261 cm^{-1}) and bending vibrations (1177 cm^{-1}) of the phenolic groups decomposed from Fe-PDA.[49,61] In LOI and UL-94 tests, the phenolic compounds (e.g., catechol) were continuously released at the early decomposition stages, which greatly contributed to the extinguishment of flame via free radical scavenging action in gas phase. In terms of cone calorimeter test, the combustion process only started after the early decomposition of EP/Fe-PDA. Rapid and fierce decomposition process happened under the forced-flaming combustion by external radiation (787 °C). Under the high temperature, the catecholamine moieties from Fe-PDA were not thermally stable and quickly turned into fuel for the flame, thus exhibiting a very limited flame retardant effect in gas phase.

To investigate the charring ability of Fe-PDA in EP during combustion, char residues of the specimens after cone calorimeter test were collected for further characterizations.

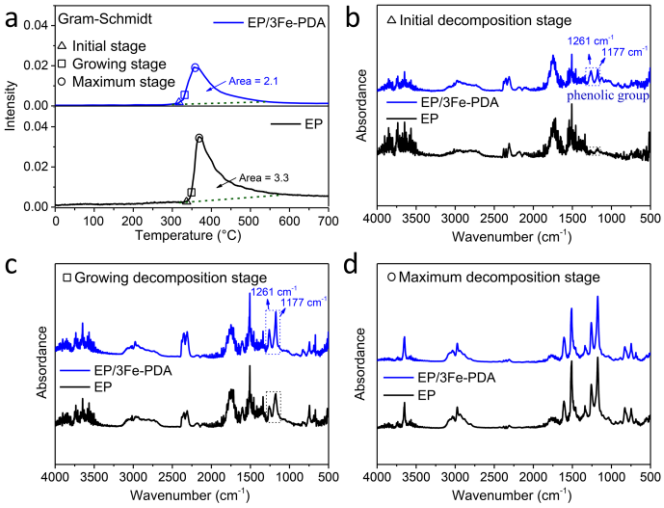

Figure 7. (a) The Gram–Schmidt curves corresponding to TG-FTIR analysis of EP and EP/3Fe-PDA, FTIR spectra of evolved gaseous products at different decomposition stages: (b) initial stage, (c) growing stage, (d) maximum stage.

Digital photos of the char residues are shown in **Figure S6**. Only a few scattered char pieces were observed for EP, while the char residues showed compact and multiple layered morphologies in the presence of Fe-PDA. SEM and Raman analysis were performed to study the microstructure and composition differences among residues from neat EP and EP composites. In contrast to neat EP (**Figure 8a**), char layers of EP/Fe-PDA nanocomposites (**Figure 8b-d**) showed a more dense morphology under SEM. Interestingly, submicron spherical particles were observed in EP/1Fe-PDA and EP/3Fe-PDA. The enlarged SEM image and Fe element mapping (**insets of Figure 8g**) revealed the particles were iron-enriched, which might be formed due to the catalytic carbonization effect of Fe-PDA. Meanwhile, microstructure differences can be observed between the residues with different flame retardant loadings in a high-magnification SEM images. EP/3Fe-PDA possessed a continuous and homogeneous morphology (**Figure 8g**) even under the high-magnification, while nano-sized pores and cracks were observed in EP/1Fe-PDA (**Figure 8f**) and EP/5Fe-PDA (**Figure 8h**), respectively. The morphology differences can

be further checked in a higher-magnification SEM images (**Figure S7**). The nano-pores in EP/1Fe-PDA can be explained by the lack of char residue due to the limited amount of flame retardant. In terms of the nano-cracks in EP/5Fe-PDA, a possible reason was the excessive metal catalysis in the composites. According to the previous literature, continuity and homogeneity of the char structures might be disrupted when the amount of metallic catalysis was above the maximum effective loading.[62] The Raman curves of char residues (**Figure 8i-l**) showed two representative peaks at 1355 and 1590 cm^{-1}, assigned to D and G peak, respectively. Ratio of the intensity of D peak to G peak (I_D/I_G) was used to evaluate the graphitization degree of char residue. The I_D/I_G value of neat EP was 2.5, whereas EP nanocomposites presented a much lower I_D/I_G value (2.1 for EP/3Fe-PDA and EP/5Fe-PDA), revealing a higher graphitization degree due to the catalytic charring effect.[63] The char residue of EP/3DOPO@Fe-PDA also showed a dense morphology with low I_D/I_G value (2.0), as seen in **Figure S8**.

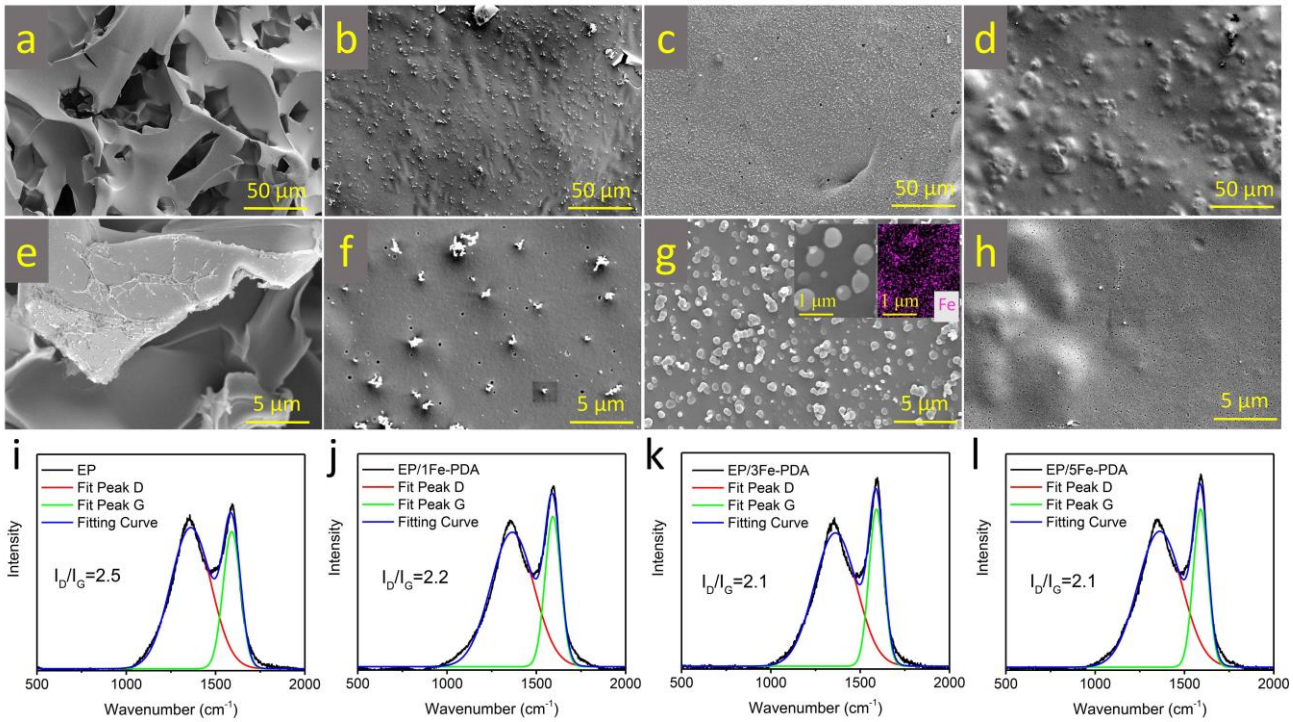

Figure 8. SEM images and Raman spectra of residues for (a,e,i) EP, (b,f,j) EP/1Fe-PDA, (c,g,k) EP/3Fe-PDA and (d,h,l) EP/5Fe-PDA.

Furthermore, TEM images of the residue pieces of EP/3Fe-PDA (**Figure 9**) clearly showed the char layer was embedded with well-dispersed iron containing nanospheres. According to XRD spectra (**Figure 9b**), different iron containing substances, like Fe_3O_4, Fe_3C and Fe were formed after combustion of the flame retardant composite. During combustion, Fe(III) in Fe-PDA nanospheres might react with nearby hydrocarbon materials, forming Fe_3C. In the presence of air and volatile products degraded from EP, it can be further oxidized to Fe_3O_4 and reduced to Fe, respectively.[64]

Based on above results and analysis, the flame retardant mechanism of Fe-PDA in EP nanocomposite is proposed in **Scheme 2**. The iron-loaded PDA nanospheres, with both free radical scavenging and catalytic charring abilities, acted as highly effective flame retardant in both gas phase and condensed phase. The combustion of polymer material strongly depended on the concentration of highly reactive radicals (like H•, OH•) that provide additional fuels to sustain the flame. Fe-PDA might slow down the radical chain reactions by scavenging nearby H•/OH• radicals, thus facilitating the extinguishment of flame. The improved LOI value and UL-94 rating of the flame retardant composites were mainly contributed to the flame inhibition action. In condensed phase, Fe-PDA effectively promoted the charring process of EP, leading to the formation of compact and dense char layers at materials surface. This

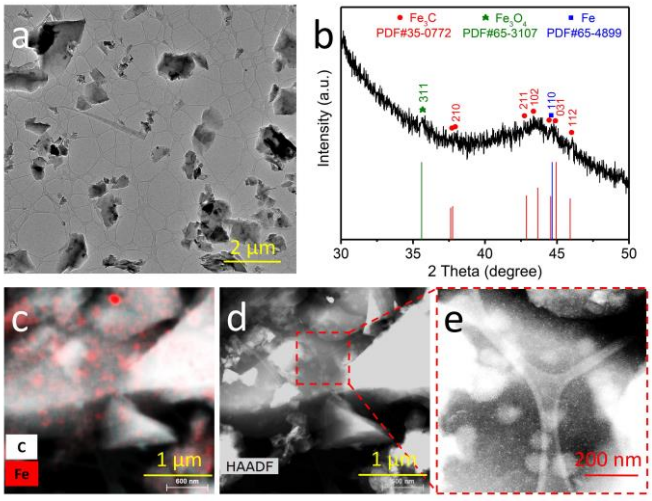

Figure 9. (a) TEM image, (b) XRD spectra, (c) C, Fe element mapping and (d,e) HAADF images of EP/3Fe-PDA residue after cone calorimeter test.

physical barrier delayed the mass and heat transfer in combustion, which significantly reduced the heat release rate of materials in cone calorimeter test.

3.4 Mechanical behaviour of EP/Fe-DPA composites

It is always desired to render EP high flame retardancy while maintaining other properties on an adequate level. In this study, dynamic mechanical analysis (DMA) and tensile test were performed to study the mechanical properties of EP

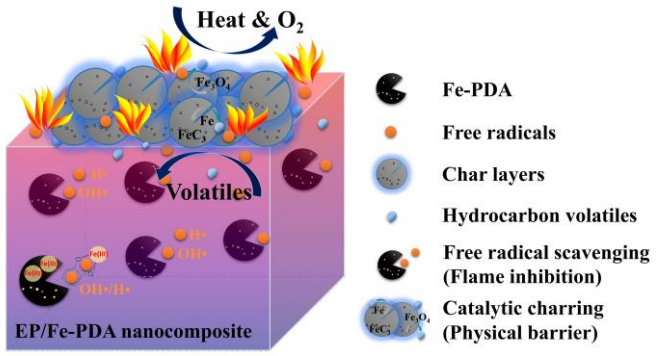

Scheme 2. Schematic illustration of flame retardant mechanism for EP/Fe-PDA nanocomposite.

nanocomposites. The storage modulus and tan delta plots of EP and its nanocomposites are shown in **Figure S9**. The storage modulus (at 30 °C), glass transition temperature (T_g, temperature at peak tan delta), as well as the tensile strength and Young's modulus are listed in **Table 2.** The storage modulus of EP (1780 MPa) was increased with the addition of Fe-PDA nanospheres, reaching to the highest at 1916 MPa for EP/3Fe-PDA. The Young's modulus of EP (1025±23 MPa) followed a similar increasing trend, though the highest (1227±62 MPa) was displayed for EP/5Fe-PDA. Besides, an obvious improvement (around 15 °C) was observed for glass transition temperature of the nanocomposites. In terms of tensile strength, a slight improvement was achieved for EP/1Fe-PDA (61.9±2.3 MPa) and EP/3Fe-PDA (60.7±3.5 MPa). However, the tensile strength dropped to 58.6±4.6 MPa for EP/5Fe-PDA, which was a little lower than 59.6±3.8 MPa for neat EP. The enhanced modulus and T_g values of EP composites could arise from the strong polymer–nanoparticle interfacial interactions.[65] The abundant catechol groups at surface of Fe-PDA greatly facilitated the formation of hydrogen bonds between epoxy resin and nanoparticles.[66] Moreover, as shown in the dynamic DSC curves of EP and its nanocomposites (**Figure S10**), the addition of Fe-PDA promoted the curing reaction of EP. The SEM images of freeze-fractured surfaces for neat EP and EP/3Fe-PDA are presented in **Figure S11**. Compared to neat EP with a relatively glossy surface, EP/3Fe-PDA exhibited an increased roughness with more cracks. Meanwhile, well dispersed nanoparticles exposed on the fracture surface were observed in the high resolution SEM image of EP/3Fe-PDA, which contributed to the mechanical enhancement of Fe-PDA in EP matrix at a certain loading level.

Table 2. DMA and tensile test results for EP and its composites.

Sample	Storage Modulus at 30 °C (MPa)	T_g (°C)	Tensile strength (MPa)	Young's modulus (MPa)
EP	1780	140	59.6±3.8	1025±23
EP/1Fe-PDA	1828	156	61.9±2.3	1183±21
EP/3Fe-PDA	1916	154	60.7±3.5	1196±45
EP/5Fe-PDA	1847	155	58.6±4.6	1227±62

4. Conclusions

In this study, the bioinspired iron-loaded polydopamine nanospheres were used as green flame retardant additives in EP composites. The flame retardancy of EP nanocomposites were significantly improved with the addition of Fe-PDA. Compared to neat EP with the LOI value of 25.6%, no rating in UL-94 test and pHRR of 1285 kW/m^2 in cone calorimeter test, EP/3Fe-PDA showed the increased LOI value of 30.5%, V-1 rating and reduced pHRR at 780 kW/m^2. On the contrary, DOPO modified Fe-PDA showed a low flame retardant efficiency in EP matrix under LOI and UL-94 tests, which well corresponded to its declined radical scavenging activity in comparison with Fe-PDA. These results suggested that Fe-PDA acted in gas phase by scavenging nearby H•/OH• radicals, thus facilitating the extinguishment of flame. In addition, the char residues for EP/3Fe-PDA showed dense and multiple layered morphologies after cone calorimeter test, due to the catalytic charring ability of Fe-PDA in condensed phase. The intensive carbonaceous layers acted as the physical barrier to protect the underlying polymeric substrate, thus effectively decreasing the heat release rate of materials. Based on these results, it is concluded that Fe-PDA can act as the nontoxic and highly efficient flame retardants in EP. This research also helps to understand why PDA coated porous materials or fabrics showed high flame retardancy in previous researches.[24-30] Furthermore, it is expected that the use of iron loaded PDA as the surface nanocoatings for various fillers could become a universal strategy to prepare high performance flame retardant polymer composites.

Conflicts of interest

There are no conflicts to declare.

Acknowledgements

This research is partly funded by joint Research Fund for Overseas Chinese, Hong Kong and Macao Young Scholars (51929301) and the financial support from China Scholarship Council (ID: 201506370020) to Mr. Lu Zhang.

References

1 H. Lee, J. Rho and P. B. Messersmith, *Adv. Mater.*, 2009, **21**, 431-434.
2 H. Lee, S. M. Dellatore, W. M. Miller and P. B. Messersmith, *Science*, 2007, **318**, 426-430.
3 S. Hong, Y. S. Na, S. Choi, I. T. Song, W. Y. Kim and H. Lee, *Adv. Funct. Mater.*, 2012, **22**, 4711-4717.
4 J. Liebscher, R. Mrówczyński, H. A. Scheidt, C. Filip, N. D. Haïdade, R. Turcu, A. Bende and S. Beck, *Langmuir*, 2013, **29**, 10539-10548.
5 L. Guo, Q. Liu, G. Li, J. Shi, J. Liu, T. Wang and G. Jiang, *Nanoscale*, 2012, **4**, 5864-5867.
6 M. J. Harrington, A. Masic, N. Holten-Andersen, J. H. Waite and P. Fratzl, *Science*, 2010, **328**, 216-220.
7 S. Chen, Y. Cao and J. Feng, *ACS Appl. Mater. Interfaces*, 2013, **6**, 349-356.
8 L. Zhang, S. Yuan, S. Chen, D. Wang, B. Z. Han and Z. M. Dang, *Compos. Sci. Technol.*, 2015, **110**, 126-131.
9 Z. Wang, M. Yang, Y. Cheng, J. Liu, B. Xiao, S. Chen, J. Huang, Q. Xie, G. Wu and H. Wu, *Compos. Part A Appl. Sci. Manuf.*, 2019, **118**, 302-311.
10 H. Yuan, Y. Wang, T. Li, Y. Wang, P. Ma, H. Zhang, W. Yang, M. Chen and W. Dong, *Nanoscale*, 2019, **11**, 11360-11368.
11 L. Yang, J. Kong, W. A. Yee, W. Liu, S. L. Phua, C. L. Toh, S. Huang and X. Lu, *Nanoscale*, 2012, **4**, 4968-4971.
12 S. L. Phua, L. Yang, C. L. Toh, S. Huang, Z. Tsakadze, S. K. Lau, Y. W. Mai and X. Lu, *ACS Appl. Mater. Interfaces*, 2012, **4**, 4571-4578.
13 H. ping Zhang, W. Han, J. Tavakoli, Y. ping Zhang, X. Lin, X. Lu, Y. Ma and Y. Tang, *Compos. Part A Appl. Sci. Manuf.*, 2019, **116**, 62-71.
14 Y. Liu, K. Ai and L. Lu, *Chem. Rev.*, 2014, **114**, 5057-5115.
15 Z. Dong, H. Gong, M. Gao, W. Zhu, X. Sun, L. Feng, T. Fu, Y. Li and Z. Liu, *Theranostics*, 2016, **6**, 1031-1042.
16 K. Ai, Y. Liu, C. Ruan, L. Lu and G. Lu, *Adv. Mater.*, 2013, **25**, 998-1003.
17 K. Y. Ju, Y. Lee, S. Lee, S. B. Park and J. K. Lee, *Biomacromolecules*, 2011, **12**, 625-632.
18 Y. Li, Y. Xie, Z. Wang, N. Zang, F. Carniato, Y. Huang, C. M. Andolina, L. R. Parent, T. B. Ditri, E. D. Walter, M. Botta, J. D. Rinehart and N. C. Gianneschi, *ACS Nano*, 2016, **10**, 10186-10194.
19 Z. Wang, Y. Xie, Y. Li, Y. Huang, L. R. Parent, T. Ditri, N. Zang, J. D. Rinehart and N. C. Gianneschi, *Chem. Mater.*, 2017, **29**, 8195-8201.
20 L. Yang, J. Kong, D. Zhou, J. M. Ang, S. L. Phua, W. A. Yee, H. Liu, Y. Huang and X. Lu, *Chem. - A Eur. J.*, 2014, **20**, 7776-7783.
21 X. Li, P. Gao, J. Tan, K. Xiong, M. F. Maitz, C. Pan, H. Wu, Y. Chen, Z. Yang and N. Huang, *ACS Appl. Mater. Interfaces*, 2018, **10**, 40844-40853.
22 A. Barik, B. Mishra, L. Shen, H. Mohan, R. M. Kadam, S. Dutta, H. Y. Zhang and K. I. Priyadarsini, *Free Radic. Biol. Med.*, 2005, **39**, 811-822.
23 J. Zhang, Q. Kong and D. Y. Wang, *J. Mater. Chem. A*, 2018, **6**, 6376-6386.
24 H. Kim, D. W. Kim, V. Vasagar, H. Ha, S. Nazarenko and C. J. Ellison, *Adv. Funct. Mater.*, 2018, **28**, 1803172
25 J. H. Cho, V. Vasagar, K. Shanmuganathan, A. R. Jones, S. Nazarenko and C. J. Ellison, *Chem. Mater.*, 2015, **27**, 6784-6790.
26 C. Ruan, K. Ai, X. Li and L. Lu, *Angew. Chemie - Int. Ed.*, 2014, **53**, 5556-5560.
27 Y. Li, B. Wang, X. Sui, H. Xu, L. Zhang, Y. Zhong and Z. Mao, *Cellulose*, 2017, **24**, 3815-3823.
28 S. Wang, X. Du, S. Deng, X. Fu, Z. Du, X. Cheng and H. Wang, *Cellulose*, 2019, **26**, 7009-7023.
29 Y. Li, B. Wang, X. Sui, R. Xie, H. Xu, L. Zhang, Y. Zhong and Z. Mao, *Appl. Surf. Sci.*, 2018, **435**, 1337-1343.
30 F. Luo, K. Wu, J. Shi, X. Du, X. Li, L. Yang and M. Lu, *J. Mater. Chem. A*, 2017, **5**, 18542-18550.
31 Z. Li, L. Liu, A. Jiménez González and D. Y. Wang, *Polym. Chem.*, 2017, **8**, 3926-3936.
32 Z. Li, S. I. Montero Lira, L. Zhang, D. F. Expósito, V. B. Heeralal and D. Y. Wang, *Polym. Degrad. Stab.*, 2018, **157**, 119-130.
33 L. Zhang, Z. Li, Y. T. Pan, A. P. Yáñez, S. Hu, X. Q. Zhang, R. Wang and D. Y. Wang, *Compos. Part B Eng.*, 2018, **154**, 56-63.
34 M. M. Velencoso, A. Battig, J. C. Markwart, B. Schartel and F. R. Wurm, *Angew. Chemie - Int. Ed.*, 2018 2018, **57**, 10450-10467.
35 B. Camino and G. Camino, *Polym. Degrad. Stab.*, 2019, **160**, 142-147.
36 J. Green, *J. Fire Sci.*, 1996, **14**, 426-442.
37 S. Wagner, M. Rakotomalala, Y. Bykov, O. Walter and M. Döring, *Heteroat. Chem.*, 2012, **23**, 216-222.
38 K. A. Salmeia and S. Gaan, *Polym. Degrad. Stab.*, 2015, **113**, 119-134.
39 J. M. Ang, Y. Du, B. Y. Tay, C. Zhao, J. Kong, L. P. Stubbs and X. Lu, *Langmuir*, 2016, **32**, 9265-9275.
40 S. L. Phua, L. Yang, C. L. Toh, D. Guoqiang, S. K. Lau, A. Dasari and X. Lu, *ACS Appl. Mater. Interfaces*, 2013, **5**, 1302-1309.
41 N. Bertrand, C. Desgranges, D. Poquillon, M. C. Lafont and D. Monceau, *Oxid. Met.*, 2010, ***73***, 139-162.
42 M. Oku and K. Hirokawa, *J. Electron Spectros. Relat. Phenomena*, 1976, **8**, 475-481.
43 A. Velázquez-Palenzuela, L. Zhang, L. Wang, P. L. Cabot, E. Brillas, K. Tsay and J. Zhang, *J. Phys. Chem. C*, 2011, **115**, 12929-12940.
44 M. Lin, H. Huang, Y. Liu, C. Liang, S. Fei, X. Chen and C. Ni, *Nanotechnology*, 2013, **24**, 065501.
45 J. Xi, Y. Xia, Y. Xu, J. Xiao and S. Wang, *Chem. Commun.*, 2015, **51**, 10479-10482.
46 N. F. Della Vecchia, R. Avolio, M. Alfè, M. E. Errico, A. Napolitano and M. D'Ischia, *Adv. Funct. Mater.*, 2013, **23**, 1331-1340.
47 M. D'Ischia, A. Napolitano, A. Pezzella, P. Meredith and T. Sarna, *Angew. Chemie - Int. Ed.*, 2009, **48**, 3914-3921.
48 M. J. Sever, J. T. Weisser, J. Monahan, S. Srinivasan and J. J. Wilker, *Angew. Chemie - Int. Ed.*, 2004, **43**, 448-450.
49 I. A. Janković, Z. V. Šaponjić, E. S. Džunuzović and J. M. Nedeljković, *Nanoscale Res. Lett.*, 2010, **5**, 81.
50 Z. Zhang, L. Yuan, G. Liang, A. Gu, Z. Qiang, C. Yang and X. Chen, *J. Mater. Chem. A*, 2014, **2**, 4975-4988.
51 B. Liu, X. Gao, Y. Zhao, L. Dai, Z. Xie and Z. Zhang, *J. Mater. Sci.*, 2017, **52**, 8603-8617.
52 C. Liu, T. Chen, C. H. Yuan, C. F. Song, Y. Chang, G. R. Chen, Y. T. Xu and L. Z. Dai, *J. Mater. Chem. A, 2016*, **4**, 3462-3470.
53 N. M. Neisius, M. Lutz, D. Rentsch, P. Hemberger and S. Gaan, *Ind. Eng. Chem. Res.*, 2014, 53, 2889-2896.
54 F. Bou-Abdallah and N. D. Chasteen, *J. Biol. Inorg. Chem.*, 2008, **13**, 15-24.
55 T. Sarna, J. S. Hyde and H. M. Swartz, *Science*, 1976, **192**, 1132-1134.
56 M. Rózanowska, T. Sarna, E. J. Land and T. G. Truscott, *Free Radic. Biol. Med.*, 1999, **26**, 518-525.
57 G. Sánchez, Z. Brito, V. Mujica and G. Perdomo, *Polym. Degrad. Stab.*, 1993, **40**, 109-114.
58 J. S. Wang, Y. Liu, H. B. Zhao, J. Liu, D. Y. Wang, Y. P. Song and Y. Z. Wang, *Polym. Degrad. Stab.*, 2009, **94**, 625-631.
59 Z. Osawa, *Polym. Degrad. Stab.*, 1988, **20**, 203-236.
60 T. Ahamad and S. M. Alshehri, *J. Hazard. Mater.*, 2012, **199**, 200-208.
61 H. Gulley-Stahl, P. A. Hogan, W. L. Schmidt, S. J. Wall, A. Buhrlage and H. A. Bullen, *Environ. Sci. Technol.* 2010, **44**, 4116-4121.

62 M. Lewin and M. Endo, *Polym. Adv. Technol.*, 2003, **14**, 3–11.
63 S. Qiu, Y. Zhou, X. Zhou, T. Zhang, C. Wang, R. K. K. Yuen, W. Hu and Y. Hu, *Small*, 2019, **15**, 1805175.
64 J. Gong, X. Chen and T. Tang, *Prog. Polym. Sci.*, 2019, **94**, 1-32.
65 P. Rittigstein, R. D. Priestley, L. J. Broadbelt and J. M. Torkelson, *Nat. Mater.*, 2007, **6**, 278-282.
66 L. Yang, S. L. Phua, J. K. H. Teo, C. L. Toh, S. K. Lau, J. Ma and X. Lu, *ACS Appl. Mater. Interfaces*, 2011, **3**, 3026-3032.